JGR Solid Earth

RESEARCH ARTICLE
10.1029/2019JB017326

Imaging Upper-Mantle Structure Under USArray Using Long-Period Reflection Seismology

Peter M. Shearer[1] **and Janine Buehler**[2]

[1]Scripps Institution of Oceanography, University of California, San Diego, La Jolla, CA, USA, [2]Now at Swiss National Science Foundation, Berne, Switzerland

Key Points:
- Common-reflection-point stacking applied to long-period teleseismic SH waves images upper-mantle discontinuities under USArray
- These images show the 410- and 660-km discontinuities as well as a negative polarity reflection between 50 and 100 km under much of the United States
- A steeply dipping structure is imaged in the western United States that could be related to the Farallon Slab

Supporting Information:
- Supporting Information S1
- Tables S1
- Tables S2
- Tables S3
- Figure S1
- Figure S2
- Figure S3
- Figure S4

Correspondence to:
P. Shearer,
pshearer@ucsd.edu

Citation:
Shearer, P. M., & Buehler, J. (2019). Imaging upper-mantle structure under USArray using long-period reflection seismology. *Journal of Geophysical Research: Solid Earth*, *124*. https://doi.org/10.1029/2019JB017326

Received 7 JAN 2019
Accepted 19 JUL 2019
Accepted article online 31 JUL 2019

Abstract Topside reverberations off mantle discontinuities are commonly observed at long periods, but their interpretation is complicated because they include both near-source and near-receiver reflections. We have developed a method to isolate the stationside reflectors in large data sets with many sources and receivers. Analysis of USArray transverse-component data from 3,200 earthquakes, using direct *S* as a reference phase, shows clear reflections off the 410- and 660-km discontinuities, which can be used to map the depth and brightness of these features. Because our results are sensitive to the impedance contrast (velocity and density), they provide a useful complement to receiver-function studies, which are primarily sensitive to the *S* velocity jump alone. In addition, reflectors in our images are more spread out in time than in receiver functions, providing good depth resolution. Our images show strong discontinuities near 410 and 660 km across the entire USArray footprint, with intriguing reflectors at shallower depths in many regions. Overall, the discontinuities in the east appear simpler and more monotonous with a uniform transition zone thickness of 250 km compared to the western United States. In the west, we observe more complex discontinuity topography and small-scale changes below the Great Basin and the Rocky Mountains, and a decrease in transition-zone thickness along the western coast. We also observe a dipping reflector in the west that aligns with the top of the high-velocity Farallon slab anomaly seen in some tomography models, but which also may be an artifact caused by near-surface scattering of incoming *S* waves.

1. Introduction

Stacks of long-period seismograms at teleseismic distances reveal a variety of secondary seismic phases resulting from reflections and phase conversions from upper-mantle discontinuities (e.g., Shearer, 1991, 1990). Of these, converted phases from interfaces below the stations (receiver functions) and underside reflections precursory to *SS* and *PP* have received the most attention and have been widely used to map the topography of the 410- and 660-km discontinuities. In contrast, topside reverberations, such as *Ss*660*s*, are obvious in data stacks (see Figure 1a) but have not been studied very much because their interpretation is complicated by the fact that they include both near-source and near-receiver reflections (see Figure 1b).

In principle, this source-receiver ambiguity can be removed given many sources and receivers and spatially variable discontinuity properties. That is, if each source is recorded by multiple stations and each station records multiple earthquakes, then one can formulate an inverse problem to separately resolve near-source and near-receiver discontinuity structure. We apply this approach here to image upper-mantle discontinuities under 1688 stations of the USArray experiment across the contiguous United States using long-period *SH*-wave reflections and a common-reflection-point (CRP) stacking method. We observe variations in the properties of the 410- and 660-km discontinuities, as well as a negative polarity reflection (NPR) at 40- to 100-km depth. In unsmoothed data, we also observe reflections from a dipping feature that agrees in position with the Farallon slab imaged in some tomography models, but which may also be an artifact related to scattering from the western continental margin.

2. Data and Method

We obtained USArray data from 2004 to 2014 for 3,200 shallow earthquakes ($M \geq 5$, depth $\leq$50 km, see Figure 2), rotated the horizontals to obtain transverse components and applied a 10-s low-pass filter. We then required that each earthquake be recorded by at least five stations with a signal-to-prearrival-noise ratio of

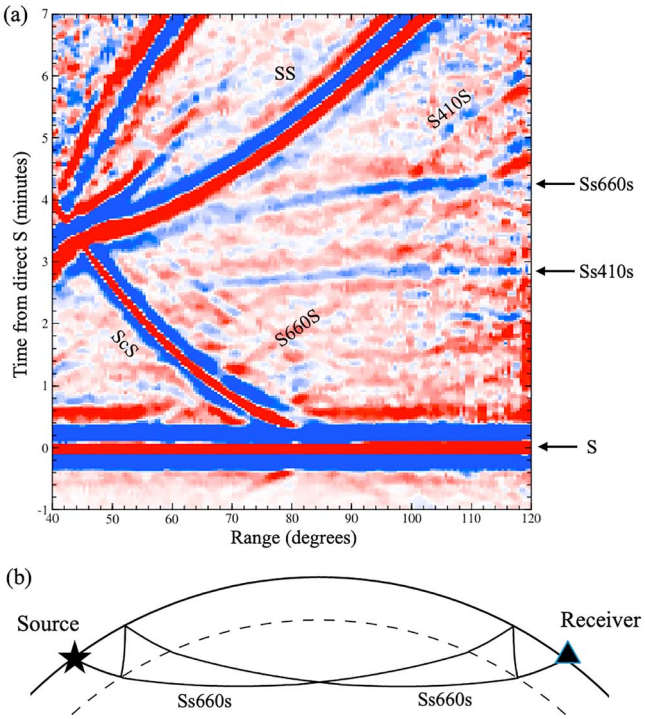

Figure 1. (a) A global stack of long-period *S* waves from shallow earthquakes (<50-km depth) and transverse-component, global seismic network data from 1976 to 2010, using direct *S* as a reference phase. Waveforms are aligned and normalized to unit amplitude using the maximum amplitude of direct *S* (or S_{diff}), flipping the polarity as needed, and stacked in 0.5° bins in epicentral distance. Positive amplitudes are plotted as red, negative amplitudes as blue, with the maximum set to 0.05 of the direct *S* amplitude. The topside reverberations, *Ss*410*S* and *Ss*660*s*, appear as blue streaks following *S* by 2.5 to 4 min. Note that their polarity is reversed from *S* because of the discontinuity reflection. Other phases, including precursors to *SS* from underside reflections (*S*410*S* and *S*660*S*), are labeled. (b) The topside 660-km reflected phase, *Ss*660*s* results from both near-source and near-receiver reverberations, as shown by raypaths for the iasp91 velocity model (Kennett & Engdahl, 1991).

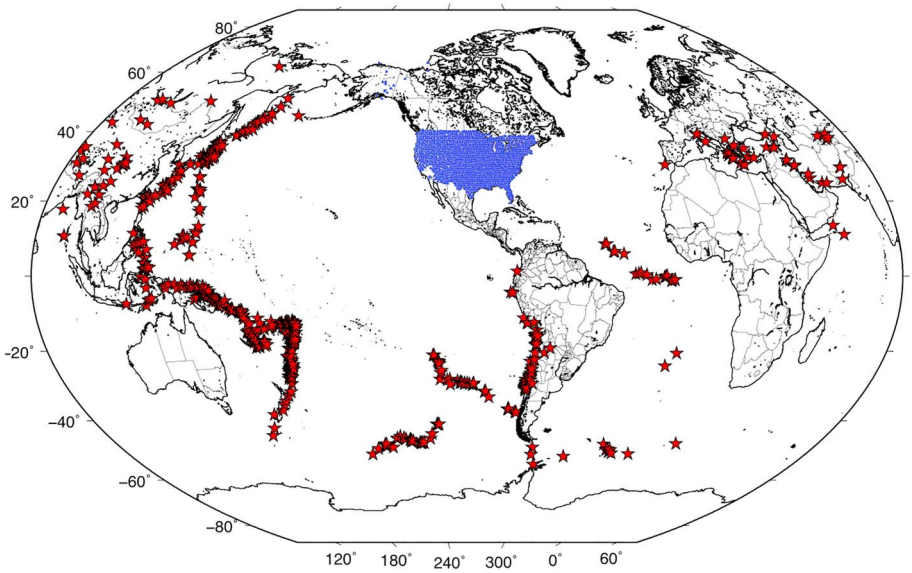

Figure 2. Sources and receivers used in this study. We examined 3,200 earthquakes of $M \geq 5.5$ and depth ≤50 km (red stars) recorded by 1,688 USArray stations (blue dots) between 75° and 120°, with 183 earthquakes remaining after our selection screening (see text).

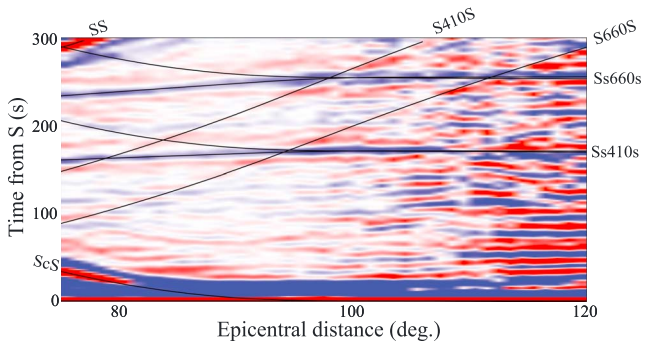

Figure 3. A record-section stack of our USArray transverse-component data, aligned and normalized on direct *S* as in Figure 1. The topside reflected phases, *Ss*410*s* and *Ss*660*s*, are labeled, as well as the underside reflected precursors to *SS*, *S*410*S*, and *S*660*S*.

5 or greaterbetween 75° and 120°. This left us with about 80,000 seismograms, which we then resampled to 1 Hz and aligned and normalized to the maximum amplitude of direct *S*. This simple waveform alignment method (e.g., Shearer, 1991) is easier to perform than reference-phase deconvolution methods (e.g., Gu et al., 1998; 2003) but produces similar results (e.g., Houser et al., 2008). Next, we examined the arrivals from each earthquake and computed two measures of the impulsiveness and amplitude of direct *S* compared to its coda between 20 and 250 s after *S*: (1) the RMS coda amplitude over all stations and (2) the average maximum coda amplitude over all stations. We rejected earthquakes if the RMS amplitude of the coda exceeded 20% of the direct *S* amplitude or if the average maximum amplitude of the coda exceeded 40% of the direct *S* amplitude. These criteria were based on visual screening of individual event record sections and were sufficient to reject events with extended source-time functions or anomalously large late arrivals. This reduced our total number of earthquakes to 183 but left over half of the original seismograms because most of the rejected events had small numbers of seismograms that survived the initial signal-to-prearrival-noise ratio cutoff.

Next, we constructed a record-section image similar to the global stack of Figure 1 by aligning and normalizing the records on direct *S* and stacking the waveforms in 1° increments in epicentral distance. As shown in Figure 3, the topside reflections *Ss*410*s* and *Ss*660*s* are clearly visible at about 160 to 260 s following direct *S*. The underside reflections *S*410*S* and *S*660*S* are also visible but are much less prominent. There is comparatively little data beyond 110° where the image is notably noisier. In subsequent processing, we use only data from 75° to 110° and also exclude data arriving within 20 s of *ScS* at less than 82° and arriving within 40 s of SS.

Assuming the ray geometry for topside reflections off horizontal discontinuities, a reference 1-D velocity model (iasp91 in this case) can be used to convert between delay time after direct *S* and reflector depth. Ignoring the source- versus receiver-side ambiguity for now, a measure of the expected horizontal resolution of these reflections is provided by the Fresnel zone. Figure 4 plots contours of traveltime increases resulting from perturbations from the Snell's law reflection point for reflectors at depths of 200, 400, and 600 km. Constructive interference occurs at times up to $T/2$, where T is the period of the data; thus, for the ~20-s dominant period of our waveforms, the Fresnel zone is defined by the 10-s contour. As expected, the Fresnel zone increases in size with depth, from about 2° across at 200 km to 6° across at 600 km. The zone is nearly circular, unlike the strange saddle-shaped traveltime surfaces resulting from *SS* and *PP* precursor bouncepoint perturbations (e.g., Deuss, 2009; Shearer, 1991).

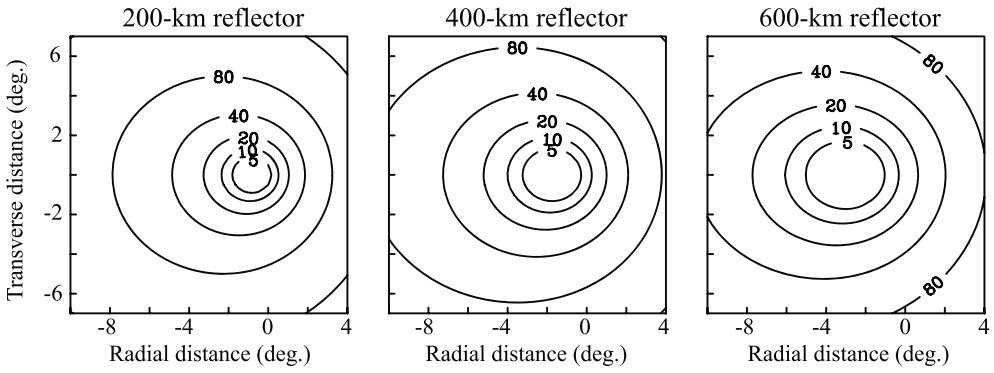

Figure 4. Fresnel zones for topside reverberations, as mapped by traveltime differences in seconds for lateral perturbations in the topside bounce points for reflectors at depths of 200, 400, and 600 km. The Snell's law reflection point is at zero time at the center of the 5-s contour. For 20-s period data, the Fresnel zone of constructive interference is defined by the 10-s contour.

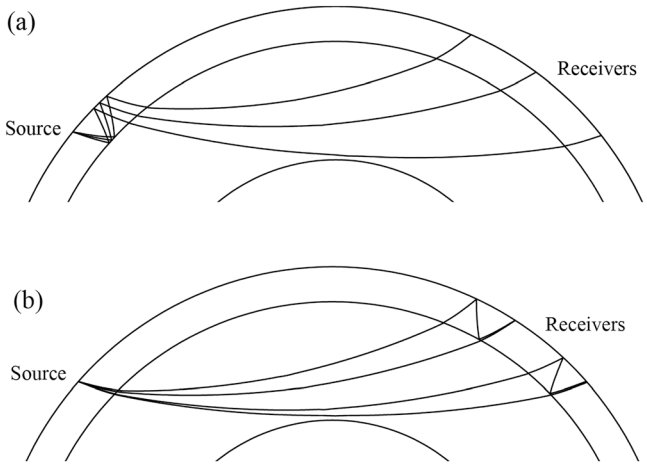

Figure 5. Raypath geometries for 660-km topside *S* wave reflections. (a) Near-source reflections observed at source-receiver distances of 75°, 87°, and 103°. (b) Near-receiver reflections compared to direct *S* at source-receiver distances of 81° and 97°. Raypaths are based on the iasp91 velocity model (Kennett & Engdahl, 1991).

For a candidate reflector depth, d, we compute the theoretical delay time of the topside-reflected phase *Ssds* compared to direct *S* for each seismogram based on its epicentral distance. The theoretical time can be computed either from a 1-D reference model or from a 3-D model if one is available (more about this later). The amplitude of the seismogram at differential time $t_{Ssds} - t_S$ can be expressed as the sum of reflections from near the source and near the receiver:

$$A_{ij}(d) = E_i(d) + C_k(d), \quad (1)$$

where A_{ij} is the observed seismogram amplitude (relative to direct *S*) for event i recorded at station j, E_i is the contribution from a near-source reflection at depth d, and C_k is the contribution from a reflection from cell k in a discretized model of a reflector at depth d under USArray. Note that all of the near-source reflection points for a given earthquake recorded by USArray are very close together, since the stations are all at similar azimuths, so a single event-specific term makes sense. In contrast, each USArray station records earthquakes at a variety of azimuths, so the discontinuity reflection points for each station will occur in different locations, which motivates a CRP stacking approach, rather than a station-term approach. Examples of ray geometries for reflections off the 660-km discontinuity are plotted in Figure 5.

We define our model as 1,586 1° rectangular cells from −130° to −70° in longitude and from 26° to 51° in latitude (see Figure 6). At each reflector depth, we set up and then solve equation (1) using an iterative least squares approach. Model points not sampled by data are set to zero. However, it is important to note that (1) contains a fundamental ambiguity in that a constant could be added to all the E_i terms and subtracted from all the C_k terms without changing the result. Thus, only relative differences in reflector properties across USArray are reliably resolved. If there was a reflector at constant depth and brightness (i.e., impedance contrast) beneath North America, we could not be sure that it truly existed, as the observed reflections could be equally interpreted as coming entirely from near-source reflections.

Figure 7 illustrates the effects of two possible ways to stabilize the inversion: (1) minimizing the receiver-side terms, that is, requiring that C_k has zero mean, and (2) minimizing all of the model terms, that is, requiring that E_i and C_k have the same average value (excluding the nonsampled model points). The left panel shows a synthetic model in which reflectors cover varying fractions of the receiver-side cells and are present (Rows

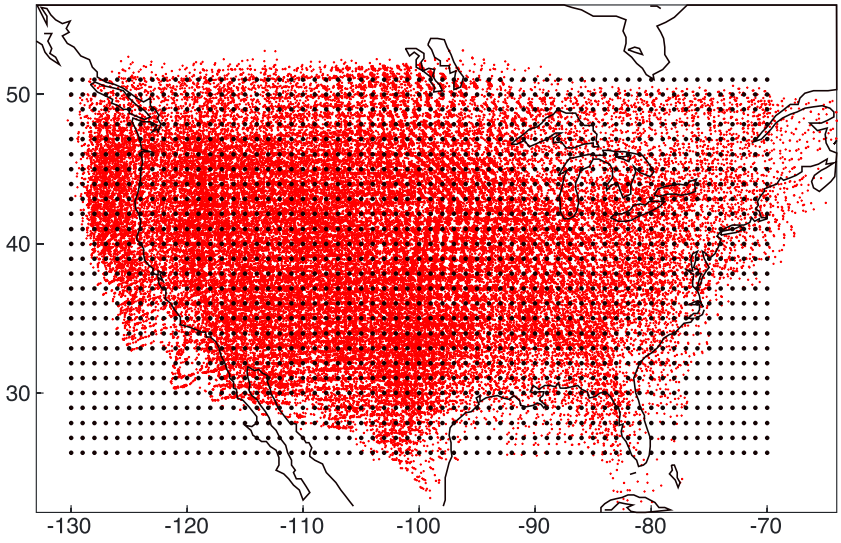

Figure 6. Our common-reflection-point model is defined by 1° latitude/longitude cells, shown as the black dots. The small red dots show predicted topside reflection points at 660-km depth for our data set; note that these are displaced from USArray station locations in the direction of the earthquake.

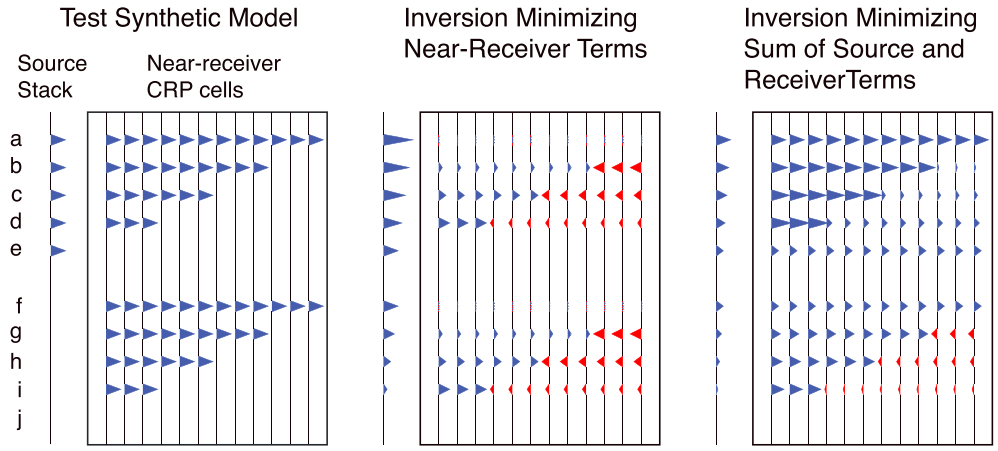

Figure 7. A simple synthetic experiment illustrating two different approaches to resolving the inversion trade-off between the source- and receiver-side contributions to the observed reflections. Positive reflectors are plotted in blue, and negative reflectors in red. The left panel shows the input model, with the source-side stack on the left and the reflections from 12 different common-reflection-point (CRP) near-receiver cells on the right.

a to e) or not present (Rows f to j) in a source-side stack. One could argue that minimizing the receiver-side terms is preferred because then any structure that remains on the receiver-side is truly required. However, this approach has the unfortunate side effect of often generating negative reflectors at the same depth as positive reflectors in other parts of the model (see middle column of Figure 7). These artifacts are reduced in our preferred approach of minimizing both the source and receiver terms (right column). This means, for example, that a uniform global discontinuity will be assigned half to the source side and half to the receiver side. A danger in our approach is that a source-side reflector could leak into the receiver terms and produce an apparent reflector where none is present (i.e., Case e). However, because our source-side stack only has significant peaks for the 410- and 660-km discontinuities, which are also present under much of USArray, this effect is unlikely to produce major artifacts in our images.

It is interesting to note that our averaging approach is a least squares (L2 norm) minimization. An L1-norm regularization would not work here. To see this, consider the case when the sum of the source and receiver contributions is one (unity). In this case, the L2-norm (least squares) solution that minimizes the source and receiver terms assigns 1/2 to each term. However, setting the source term to any value, x, between 0 and 1 and setting the receiver term to $1 - x$ will yield the same L1-norm sum. Thus, there is no well-defined best fitting L1-norm solution. Unfortunately, there is also no easy solution to the problem of positive and negative anomalies at the same depth in the receiver terms canceling out, such as forcing the receiver terms to be positive, which will not compromise the ability to resolve negative polarity reflectors. These issues warrant further study.

For our USArray data set, we solve equation (1) separately at 5-km depth increments ranging from 5 to 800 km. This produces a relatively noisy image for the 1° cells, so for most of the results presented here, we then apply horizontal smoothing to the model using a radially symmetric $\cos^2$ taper of 3° radius.

3. Results

Figure 8 plots cross-sections of the smoothed model at 2° increments in latitude and 5° increments in longitude. We define positive-polarity reflections as those indicative of positive S impedance increases with depth (e.g., Moho, 410, 660) and plot them in blue. NPRs implying impedance decreases are plotted in red. To focus on the most reliably resolved parts of the model, points are only plotted if at least 200 seismograms contribute to the model point. Although there are hints of possible reflectors at many depth and locations, we will focus on the main features: the 410- and 660-km discontinuities and a NPR imaged at about 50- to 100-km depth. Note that the 410- and 660-km discontinuities are clearly seen throughout the eastern United States and are nearly uniform in depth, but these discontinuities appear more complicated in the western United States (WUS). We experimented with low-pass filtering the data at 20-s (i.e., longer periods than the

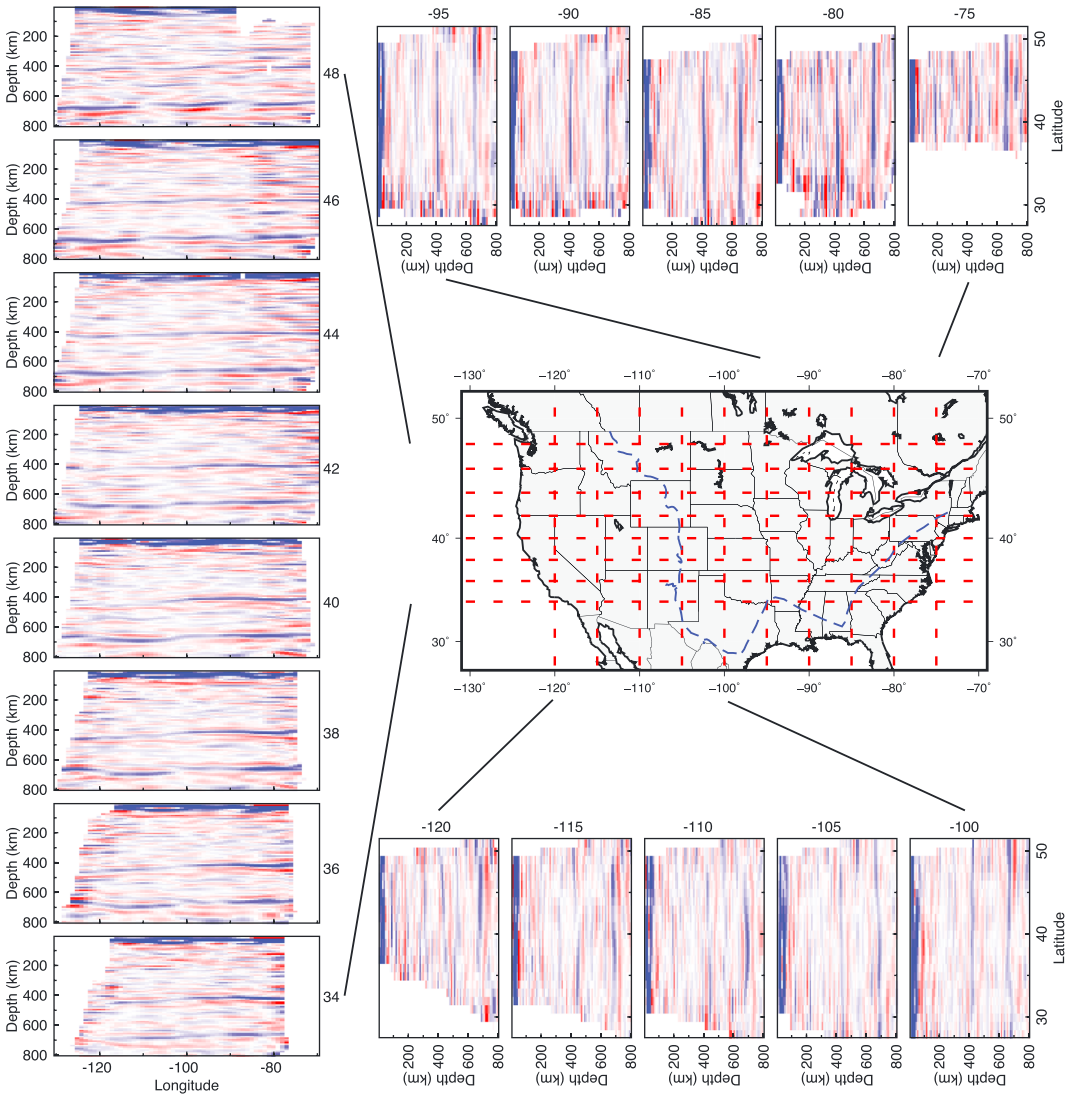

Figure 8. *S* wave reflection seismic profiles across USArray, with E-W cross-sections plotted on the left and N-S cross-sections along the top and bottom. The dashed red lines on the map show the profile locations. Positive polarity reflections, shown in blue, represent impedance increases with depth (e.g., the prominent reflections from the 410- and 660-km discontinuities). Negative polarity reflections, shown in red, represent impedance decreases with depth. Note that direct *S*, under this plotting convention, has negative polarity (see Figure 1). Maximum amplitudes (darkest blue and red) are 5% of the direct *S* wave amplitude. Vertical exaggeration is 2.9× and 2.1× for the constant latitude and longitude profiles, respectively.

10-s low pass) and found that similar features were seen (see Figure S1). However, because the reflectors are imaged more sharply in depth using the 10-s filter, we have focused on these results here.

Because this image is produced assuming a 1-D model, the depths to the reflectors may be biased by 3-D velocity structure. In particular upper-mantle *S*-velocity variations between the surface and the topside reflections (see Figure 5) will directly affect discontinuity depth estimates. We therefore repeated our analysis using ray-theoretical timing corrections estimated from the upper-mantle *S* wave tomography model of Schmandt and Lin (2014). These corrections have a significant effect, yielding changes in depths to the transition-zone discontinuities of 10 km or more in some regions (see Figure S2). However, the 3-D-corrected images appear overall somewhat less coherent than the 1-D-corrected images, while the gross features remain largely intact, so we have chosen to focus on the 1-D images here and defer to future work a detailed consideration of different tomography models and what their velocity perturbations imply for our reflector depths.

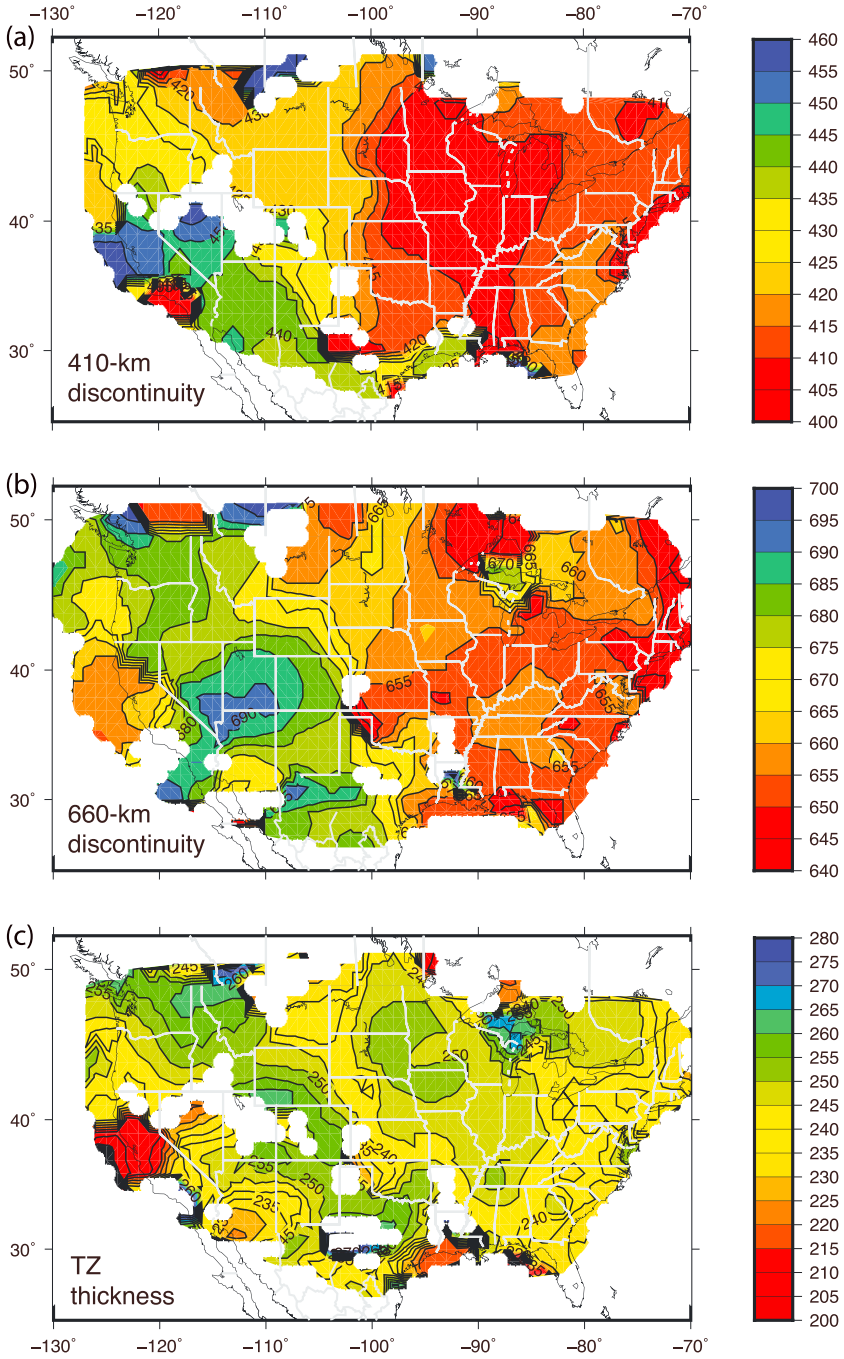

Figure 9. Topography of the (a) 410-km and (b) 660-km discontinuities, as imaged from long-period *S* wave reflections. Areas without clear reflections (see text) are plotted in white. The transition zone thickness (c) is the difference between the 410- and 660-km depths. Contours are at 5-km depth increments.

We note that such an analysis should also consider whether lower-mantle velocity variations could bias the apparent discontinuity depths, given that the raypaths of direct *S* and the topside reflections will increasingly diverge for deeper reflector depths (see Figure 5). Note that these lower-mantle raypath differences are much greater in our case than the raypath differences for receiver-function studies of upper-mantle discontinuities, so the biasing effects are likely to be more significant. A 3- to 4-s change in the differential time between direct *S* and the topside reflection in our data set will cause roughly a 10-km change in the apparent depth to the 410- and 660-km discontinuities. Direct-*S* traveltime perturbations from 3-D mantle structure are generally between ±5 s (e.g., Bolton & Masters, 2001), but average variations for nearby raypaths will be

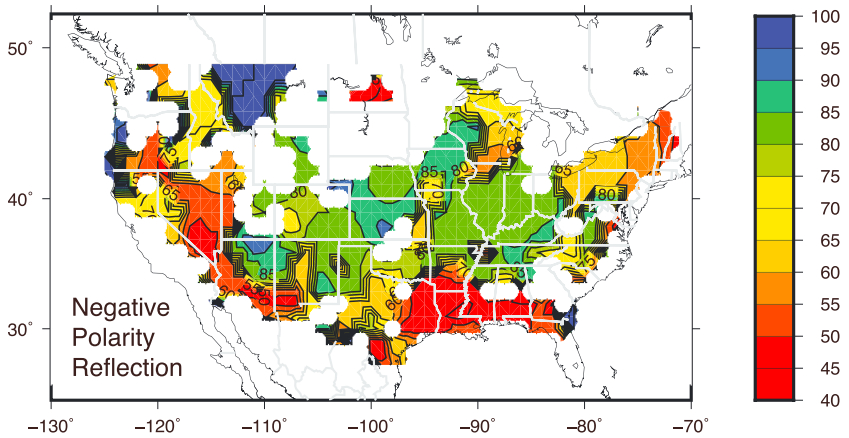

Figure 10. Depths to a negative polarity reflection observed between 40 and 100 km under much of USArray. Contours are at 5-km depth increments.

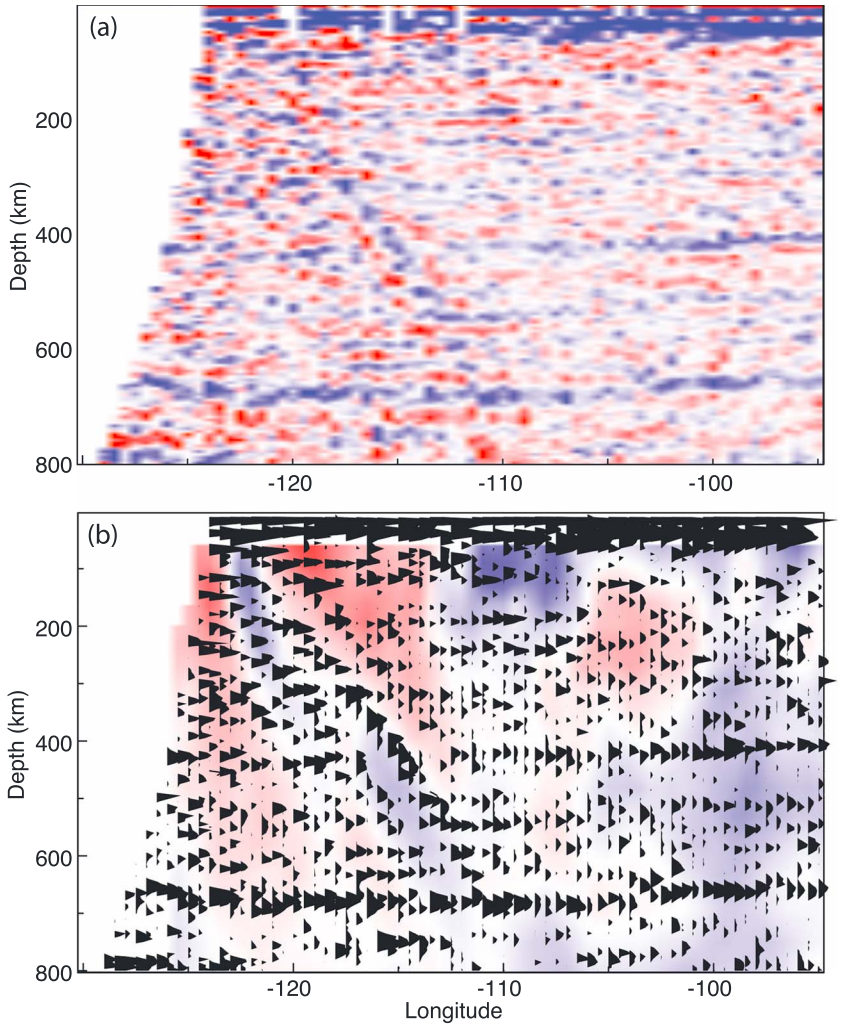

Figure 11. (a) An E-W reflection profile at 42° latitude, showing an apparent dipping reflector. N-S smoothing has been applied, but no E-W smoothing. Colors are as in Figure 8. (b) A comparison between the positive polarity reflections and the *P* wave tomography model of Schmandt and Lin (2014) at 42° N. Fast velocity anomalies are plotted in blue, negative anomalies in red. Vertical exaggeration is 2.3×.

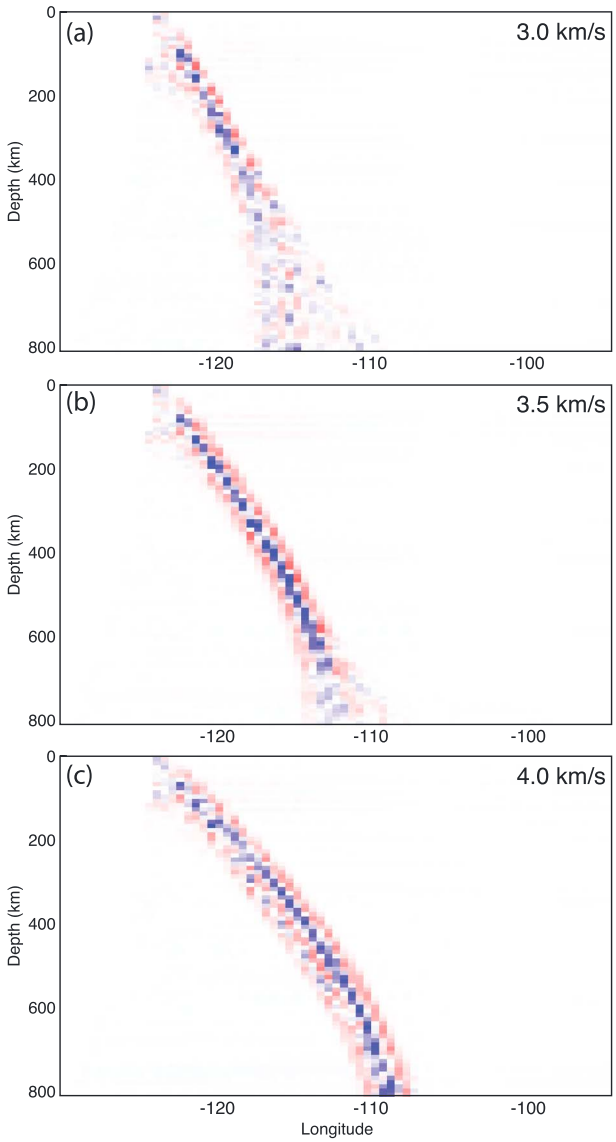

Figure 12. E-W profiles at 42° latitude obtained from inversion of synthetic data generated assuming a point scatterer near the coastline that converts incoming teleseismic *S* waves to surface waves, which then travel to the USArray stations at velocities of (a) 3 km/s, (b) 3.5 km/s, and (c) 4 km/s. Note the dipping feature that is similar to that seen in Figure 11a. Vertical exaggeration is 2.3×.

much less. For our results, the largest biasing effects from midmantle structure will occur when the raypaths graze the boundary of an anomaly bounded by sharp shear-velocity gradients. For large low shear-wave velocity provinces in the lower mantle, traveltime variations of up to 5 s are observed to occur over relatively short distances (e.g., Ritsema et al., 1998; Zhao et al., 2015), which could cause about a 15-km change in apparent transition-zone discontinuity depths.

3.1. The Transition Zone Discontinuities

To estimate transition-zone discontinuity depths, we searched for the peak amplitude from 400–460 km and 640–700 km (the approximate range spanned by the 410- and 660-km reflectors imaged in Figure 8), using spline interpolation to achieve finer depth resolution than the 5-km model spacing. We required 200 or more contributing seismograms per model point and a peak amplitude at least 1.2% of the direct *S* amplitude. Figure 9 plots the resulting topography on the 410- and 660-km discontinuities, as well as their difference (commonly termed the transition zone thickness). These apparent reflector depths are available in the electronic supplement. Both the 410- and 660-km discontinuities are fairly flat east of about −100° longitude

but deepen and appear more complex in the WUS. For the complete model, the median 410 and 660 depths (d_{410} and d_{660}) are 417 and 661 km, respectively, with a median transition-zone thickness of 245 km. These values are very close to the average discontinuity depths estimated from global *SS* precursors (e.g., 418 and 660 km from Flanagan & Shearer, 1998) and the USArray receiver function analysis of Gao and Liu (2014), who obtained average depths across the United States of 416 and 667 km. Wang and Pavlis (2016) obtained slightly different USArray receiver-function average depths of 415 and 660 km; they attributed their shallower d_{660} to their use of the AK135 reference 1-D model rather than iasp91 (their application of timing corrections based on the 3-D *P* wave model of Burdick et al., 2014, may also have been a contributing factor).

For comparison to the maps presented here, Figure S4 plots discontinuity topography results from the USArray receiver-function study of Gao and Liu (2014). In general, the depth variations agree reasonably well for the 410- and 660-km topography, but their transition zone thickness map shows much less variation than our results. We do not yet understand the source of these differences, but one possibility is that the topside *S* results are biased by unaccounted for 3-D velocity variations in the lower mantle, which are less of a concern for receiver functions (see Figure 5 and the discussion above). A full comparison to previous models and greater consideration of 3-D velocity variations will be a topic of future work.

Following Gao and Liu (2014), we use longitude −102° to separate the WUS from the central and eastern U.S. (CEUS). For our model, the CEUS has median d_{410} and d_{660} of 411 and 655 km (median TZ thickness 245 km), whereas the WUS has 431 and 678 km (median TZ thickness 246 km). Again, these values are similar to the USArray receiver function results of Gao and Liu (2014), who obtained averages of 410, 661, and 251 km for the CEUS and 425, 674, and 249 km for the WUS (uncorrected for 3-D structure). Other western USArray receiver-function analyses include Tauzin et al. (2013), who obtained average depths of 424 and 676 km, and Cao and Levander (2010), who reported average depths of 425 and 678 km.

Our results, as well as previous receiver-function analyses, indicate that average d_{410} and d_{660} estimates both increase overall by about 20 km in the west, such that their difference remains nearly constant. As argued by Gao and Liu (2014) and Wang and Pavlis (2016), this suggests the possibility that 3-D velocity structure above the 410 is biasing both discontinuities in the same direction. However, previous studies have differed regarding whether existing 3-D tomography models are sufficient to explain all of the observed discontinuity deepening in the WUS, an issue complicated by the damping applied in tomographic inversions (which reduces the amplitude of the velocity anomalies) and uncertainty in the *P* to *S* velocity scaling parameter used in some studies to generate *S* velocity perturbations from the *P* wave tomography model. Our 3-D-velocity-corrected discontinuity depths, based on the Schmandt and Lin (2014) *S* model (see the supporting information), do not substantially lessen the 20-km WUS/CEAS difference in average depths.

Noteworthy transition-zone features seen in Figures 8 and 9 include the following:

1. The apparent western deepening of the 410 occurs near −100° longitude, whereas the deepening of the 660 occurs along a NNW/SSE trending boundary that approximately coincides with the Rocky Mountain Front.
2. A pronounced depression is seen in the 660 centered on Utah with maximum depths in southern Utah, which roughly agrees in position with the sharp, localized 660 depression imaged in the receiver-function analysis of Cao and Levander (2010) and a broader depression seen in Wang and Pavlis (2016). However, other USArray receiver-function studies (Gao & Liu, 2014; Schmandt et al., 2012) have not resolved this feature.
3. The 410-km reflector nearly disappears near 40° latitude under Nevada, Utah, and western Colorado. As seen in the 40° latitude depth profile in Figure 8, this is accompanied by an apparent negative-polarity reflector at about 480-km depth. However, receiver-function studies (e.g., Cao & Levander, 2010; Cheng et al., 2017; Gao & Liu, 2014; Schmandt et al., 2012; Tauzin et al., 2013) image a 410-km reflector in this region.
4. There is a hint of a double 660-km discontinuity near 36° latitude and −105° longitude in which a reflector near 640 km seems to mirror a depression in the 660 below. This feature is more prominent in the 3-D-model-corrected image (see the supporting information). However, we could not identify a similar feature in published receiver-function profiles.
5. Near the west and gulf coasts, there are some abrupt changes in the imaged discontinuity depths. These suggest a shallowing of the 660 and a thinner transition zone off northern California and a deeper 410

and a thinner transition zone off Texas. However, because there are fewer reflection points near the edge of our model in these regions, the reliability of these features is questionable.

3.2. Possible Anomalous Features Near the 410 and 660?

Previous USArray receiver-function studies have identified some additional features near the 410- and 660-km discontinuities, including a low-velocity layer just above the 410-km discontinuity in some regions (e.g., Hier-Majumder & Tauzin, 2017; Schmandt et al., 2011; Tauzin et al., 2013) and sharp decreases in seismic velocity below the 660-km discontinuity (Schmandt et al., 2014). Both features have been interpreted as indicative of partial melt related to hydration of mantle rock.

We searched for such features in our results, that is, for negative polarity reflectors just above 410 km or just below 660 km. Examples of such anomalies can be seen in the reflectivity cross-sections plotted in Figure 8. However, we could not identify any systematic spatial correlation of such features with those described by previous authors. Although finding such a correlation might have helped validate our images, the lack of a correlation may not be significant, given differences in spatial resolution and the negative polarity artifacts that are sometimes seen in our images at the same depth as positive polarity reflectors in other parts of the model. Note that this is more of an issue for negative-polarity reflectors near the 410- and 660-km discontinuity than for the more isolated negative-polarity feature described in the next section.

3.3. The negative-polarity reflector (NPR) at 40 to 100 km

A prominent negative-polarity reflector is visible at depths between about 40 and 100 km under much of the United States. Following a similar mapping procedure to that described above for the 410 and 660, we searched for the largest negative-polarity peak in our smoothed model between 40- and 100-km depth with an amplitude at least 2% of the direct *S* amplitude. These apparent reflector depths are available in the electronic supplement. Figure 10 plots the resulting topography on what we term the NPR. It appears at about 80-km depth under much of the central United States, but shallows to about 50 km to the west, south, and northeast.

This feature has been observed in many receiver-function studies of the United States (e.g., Abt et al., 2010; Ford et al., 2016, 2014; Hansen et al., 2015; Hopper & Fischer, 2015; Kind et al., 2012; Kumar et al., 2012; Levander et al., 2011; Levander & Miller, 2012; Lekić & Fischer, 2014; Liu & Gao, 2018; Rychert & Shearer, 2009). In the tectonically active west it is usually interpreted as the top of the lithosphere-asthenosphere boundary. In the cratonic east, it has sometimes been termed the mid-lithospheric discontinuity because it appears much shallower than the thick cratonic lithosphere inferred from seismic tomography and heat flow measurements (e.g., Selway et al., 2015; Yuan et al., 2011). However, its origin in the east is unclear, and it remains somewhat mysterious that it often appears as a nearly continuous feature from west to east (e.g., Hansen et al., 2015; Kumar et al., 2012; Liu & Gao, 2018). For this reason, we prefer the term NPR because it describes the observation without making any assumptions regarding its cause.

Despite the horizontal smoothing we apply to our images, the NPR is observed intermittently in many regions and is weak or absent over much of the northern plains (see Figure 10). We see a hint of a depression in the NPR centered on southern Utah that was first noted in the WUS by Levander et al. (2011), Levander and Miller (2012), and Lekić and Fischer (2014), and which can also be seen in the recent wider-scale maps of Hansen et al. (2015) and Liu and Gao (2018). Overall, our NPR map agrees most closely with the negative velocity gradient (NVG) map of Hansen et al. (2015; see their Figure 5), particularly in the southwest, although there are also notable differences in some areas. Many of these are related to the fact that Hansen et al. (2015) include features below 100-km depth in their NVG map. Although we sometimes see deep NPRs (see Figure 8), they are generally weaker than the shallower NPR, and they do not appear as a continuous reflector, or one that deepens clearly from the shallower NPR. Thus, including them in our map would generate discontinuous jumps between depths.

In the northern Great Plains, Hopper and Fischer (2015) and Foster et al. (2014) both identify NVG features at 70–100 km, in a region where we do not image clear NPR features at similar depths. Foster et al. (2014) see two NVG features east of what they term the American Midwest transition near −96° longitude, one at about 100 km and the other at 200 to 240 km, which they interpret as the lithosphere-asthenosphere boundary. Although we observe a NPR near −90° longitude at about 180 km in our 48° latitude profile (see Figure 8), we do not observe a NPR that agrees with that imaged in Figure 2 in their paper.

3.4. Imaging the Farallon slab?

Tomographic modeling has imaged high-velocity anomalies under the WUS that have been interpreted as pieces of the subducted Farallon slab (e.g., Burdick et al., 2014; James et al., 2011; Obrebski et al., 2010, 2011; Porritt et al., 2014; Sigloch, 2011), and some receiver-function studies have also imaged parts of subducting slabs in the WUS (Cheng et al., 2017; Pavlis et al., 2012; Tauzin et al., 2013, 2016). Some of the E-W profiles plotted in Figure 8 show hints of eastward dipping structures in the WUS. However, any dipping features will be obscured by the horizontal smoothing (circular $\cos^2$ taper of 3° radius) that we apply to these images. To test whether unsmoothed images might reveal more, we repeated our inversion using model cells of 0.5° by 0.5° rather than 1° and plotted the results without horizontal smoothing. Many of the resulting E-W cross-sections show apparent dipping structures in the west but are very noisy. As the structures appear to be similar in the N-S direction, clearer results can be obtained by applying N-S smoothing. Figure 11 shows an E-W profile at 42° latitude, with N-S smoothing over model points with identical longitude using a $\cos^2$ taper of 3° radius.

This image shows a reflector that dips at about 30° between about 200 and 500 km and somewhat more steeply from 500 km to the 660-km discontinuity. Note that the true dip is shallower than the apparent dip in the image because of the vertical exaggeration of 2.3×. A comparison to the Schmandt and Lin (2014) *P* wave tomography model along the same profile (see Figure 11b) shows that this reflector aligns with the top edge of a high-velocity dipping feature, particularly between 400 and 650 km. Given this apparent correlation between our dipping reflector and the high-velocity anomalies in the Schmandt and Lin (2014) model, it is tempting to argue that we are imaging the top of the subducted Farallon slab. However, caution is warranted for several reasons. Tomography models differ in their details, including the position of the high-velocity upper-mantle anomalies in the WUS (e.g., Burdick et al., 2014; James et al., 2011; Obrebski et al., 2010, 2011), and we do not always image reflectors at the top of fast "blobs" in the models, including those seen in other cross-sections through the Schmandt and Lin (2014) model. Indeed, our slab does not agree in position with the inferred slab location in the Pavlis (2011) migrated receiver-function study or the slab position in the tomography/receiver-function synthesis of Pavlis et al. (2012). In addition, our images are unmigrated, and dipping reflectors may not be imaged in the correct position using CRP stacking, even without additional horizontal smoothing.

Finally, there is the possibility that this dipping feature is some kind of artifact related to scattering of incoming *S* waves off the western continental margin, such as the surface-wave scattering observed by Yu et al. (2017) and Buehler et al. (2018), that is, a feature analogous to a diffraction hyperbola in reflection seismology. To test this idea, we generated a synthetic data set in which we replaced each of our observed seismograms with simple Ricker pulses at offset times from direct *S* that were derived from the sum of the predicted iasp91 source-to-scatterer time and a scatterer-to-receiver time computed from an assumed surface-wave velocity. We then processed the synthetic data in the same way as the real data. For comparison to the cross-section plotted in Figure 11, we considered a surface scatterer at 42° N and 124° W, that is, near the western coastline. The resulting images are shown in Figure 12 for three different assumed surface-wave velocities. Because most of the incoming *S* waves for the WUS come from the west, the scatterer generates secondary waves that are increasingly delayed for stations to the east. These arrivals, when interpreted as topside reflections, will produce an apparent eastward dipping structure. For a surface-wave velocity of 3 km/s (the velocity observed for the scattered Rayleigh waves in USArray by Buehler et al., 2018, and the approximate Rayleigh-wave group velocity in the WUS from Moschetti et al., 2007, at 10- to 25-s period), the resulting image artifact is fairly sharp above 400 km but spreads and blurs below. Sharper artifacts at depth can be generated by assuming faster surface-wave velocities, which in this case serve as a rough proxy for scattered *S* body waves as 3.9 km is a typical mantle Sn velocity. In this case, the best match to the observations is obtained assuming 3.5 km/s.

However, our analysis at this point is only suggestive, as we have not tested different scatterer locations or depths or considered the more realistic possibility of multiple scatterers along the U.S. western margin. In addition, our simple synthetics have arbitrary amplitude, so we cannot be sure that scattering will yield amplitudes comparable to the observations. But given that obvious *S*-to-Rayleigh scattering is observed for some western Pacific earthquakes recorded by USArray (Buehler et al., 2018), scattered arrivals are likely present at a low level even when they are not seen directly (our signal-to-noise screening criteria exclude 17 of the 21 events identified by Buehler et al., 2018, as having scattered surface waves; manually excluding the remaining four events does not noticeably change our results). Since our synthetics indicate that such

energy may indeed produce eastward dipping features when processed using our CRP approach, we believe it would be premature to conclude that we are seeing Farallon slab reflections, even if we do not yet have a completely satisfactory explanation for our observations. Thus, for now we prefer to simply note the presence of this apparent dipping reflector in our data and defer more detailed analyses to future work.

4. Discussion

It should be noted that we are not the first to analyze topside reverberation data or the first to find evidence for dipping reflectors in the WUS. Bostock et al. (2001) and Rondenay et al. (2001) described a 2-D migration method that utilized both *P*-to-*S* conversions and topside multiples to image Cascadia subduction. Recently, Tauzin et al. (2013, 2016) and Cheng et al. (2017) used receiver-function migration to image the subducting Gorda plate to transition zone depths, and hints of Farallon slab fragments are also seen in the plane-wave migration model PWMIG11 (Pavlis et al., 2012). In addition, a migration-based approach to analysis of teleseismic free-surface multiples was recently described by Burdick et al. (2013). However, to our knowledge, we are the first to analyze topside SH reverberation data by explicitly removing the source-side terms and to apply this approach to image mantle structure under a regional seismic array.

Although complicated by the need to remove contamination for near-source structure, applying reflection-seismology methods to SH reverberation data has some advantages over traditional *Ps* and *sP* receiver function methods for imaging upper-mantle discontinuities. Because the reflections are sensitive to the two-way *S* traveltime, rather than the *S*-*P* time, reflectors are much more separated in time, which provides better depth resolution and the ability to resolve more finely spaced reflectors. They also do not suffer from the ambiguity between converted phases and reverberations that creates problems for *Ps* receiver functions at some interface depths. However, unlike receiver functions, useful SH reverberation results cannot be obtained from single stations because the source versus receiver ambiguity in the reflected phases can only be resolved through inversion of a large data set with multiple receivers. In addition, conversion of topside SH reflection times to depth is more likely affected by biases from mantle 3-D velocity structure than is the case for receiver functions because of the greater raypath separation of the direct and discontinuity phases (see Figure 5). Note that the possible biasing effect grows with discontinuity depth and is likely more important for the transition-zone discontinuities than for the NPR seen in our images at 40- to 100-km depth.

In principle, similar approaches to our method could be used to analyze topside *P* reverberation data, although such analyses would be complicated by the presence of SV phases from receiver-function conversions and reflections (e.g., Bostock et al., 2001; Rondenay et al., 2001). Of course, these additional phases could also be used to help resolve the source versus receiver ambiguity that we discuss here. By analyzing multiple phases, it should also be possible to separately resolve *P* velocity, *S* velocity, and density jumps at interfaces. Note that receiver functions are primarily sensitive to *S* velocity changes, while reflected phases, such as the topside SH reflections analyzed here, are mainly sensitive to impedance changes.

Our common-conversion-point (CRP) approach for teleseismic SH reverberation analysis is simple to implement and appears to give robust results for the USArray data set. However, our method likely could be improved in a number of ways:

1. Bootstrap resampling of the waveforms would provide a measure of the statistical significance of any observed reflections and could be used to replace our requirement of at least 200 seismograms to display the result.
2. In principle, migration approaches, such as those described by Pavlis (2011), Shang et al. (2012), Shragge et al. (2006), and Burdick et al. (2013) for receiver functions and/or free-surface multiples, could be applied to better image dipping structures. However, migration methods work best with uniform data coverage, so the very uneven distribution of earthquake sources may present challenges.
3. More comprehensive testing of corrections for 3-D velocity structure would help to better understand their sensitivity to specific tomography models and how they can change the coherence of the image. Ultimately, it may be desirable to perform joint inversions for 3-D structure and boundary perturbations.
4. Analysis of the radial wavefield to assess possible leakage of *P*/*SV* phases into the transverse component, which could generate artifacts in our images. Such a mechanism was proposed by Zheng and Romanowicz (2012) to explain anomalous *SS* precursor observations of the 660-km discontinuity.

5. Ray-theoretical corrections for geometrical spreading and Q models could be computed to yield more accurate estimates of the reflector amplitude and inferred reflection coefficients.
6. As suggested by Figure S1, filtering the data to longer periods might yield more coherent images of upper-mantle reflectors, at the cost of losing some depth resolution.
7. Phase-weighted or *n*th root stacking approaches might provide more robust results, although with the disadvantage that reflector amplitude variations would be harder to interpret.
8. In regions of dense and distributed seismicity, one could adapt the method to image discontinuity structure under the source region.

Of these points, perhaps the most urgent is to better understand the effect of 3-D velocity variations on our results, by considering existing tomography models for both the upper and lower mantle, because this will help inform comparisons with existing discontinuity models and help point toward the origins of the reflector topography and other variations that we observe.

Of course, the quality of our images was made possible by the incredible data coverage and quality of the USArray transportable array experiment. Similar results should be possible in other parts of the world that enjoy dense seismic array coverage, providing a useful complement to receiver function studies of upper-mantle discontinuities.

Acknowledgments
We used data from the USArray Transportable Array (TA), which are freely available as part of the EarthScope USArray facility, operated by Incorporated Research Institutions for Seismology (IRIS) and supported by the National Science Foundation, under Cooperative Agreement EAR-1261681. To access the data, go to www.usarray.org/researchers/data. Files with apparent depths to the 410-km, 660-km, and NPR discontinuities are available in the electronic supplement. Funding for this research was provided by NSF Grants EAR-1358510 and EAR-1829601.

References

Abt, D. L., Fischer, K. M., French, S. W., Ford, H. A., Yuan, H., & Romanowicz, B. (2010). North American lithospheric discontinuity structure imaged by Ps and Sp receiver functions. *Journal of Geophysical Research*, *115*, B09301. https://doi.org/10.1029/2009JB006914

Bolton, H., & Masters, G. (2001). Travel times of p and s from the global digital seismic networks: Implications for the relative variation of p and s velocity in the mantle. *Journal of Geophysical Research*, *106*(B7), 13,527–13,540.

Bostock, M., Rondenay, S., & Shragge, J. (2001). Multiparameter two-dimensional inversion of scattered teleseismic body waves 1. Theory for oblique incidence. *Journal of Geophysical Research*, *106*(B12), 30,771–30,782.

Buehler, J., Mancinelli, N., & Shearer, P. (2018). S-to-Rayleigh wave scattering from the continental margin observed at USArray. *Geophysical Research Letters*, *45*, 4719–4724. https://doi.org/10.1029/2017GL076812

Burdick, S., de Hoop, M., Wang, S., & Hilst, R. V. D. (2013). Reverse-time migration-based reflection tomography using teleseismic free surface multiples. *Geophysical Journal International*, *196*, 996–1017.

Burdick, S., Van der Hilst, R. D., Vernon, F. L., Martynov, V., Cox, T., Eakins, J., & Pavlis, G. L. (2014). Model update January 2013: Upper mantle heterogeneity beneath North America from travel-time tomography with global and USArray Transportable Array data. *Seismological Research Letters*, *85*, 77–81.

Cao, A., & Levander, A. (2010). High-resolution transition zone structures of the Gorda Slab beneath the western United States: Implication for deep water subduction. *Journal of Geophysical Research*, *115*, B07301. https://doi.org/10.1029/2009JB006876

Cheng, C., Bodin, T., Tauzin, B., & Allen, R. M. (2017). Cascadia subduction slab heterogeneity revealed by three-dimensional receiver function Kirchhoff migration. *Geophysical Research Letters*, *44*, 694–701. https://doi.org/10.1002/2016GL072142

Deuss, A. (2009). Global observations of mantle discontinuities using SS and PP precursors. *Surveys in geophysics*, *30*(4-5), 301–326.

Flanagan, M. P., & Shearer, P. M. (1998). Global mapping of topography on transition zone velocity discontinuities by stacking SS precursors. *Journal of Geophysical Research*, *103*, 2673–2692.

Ford, H. A., Long, M. D., & Wirth, E. A. (2016). Midlithospheric discontinuities and complex anisotropic layering in the mantle lithosphere beneath the Wyoming and Superior Provinces. *Journal of Geophysical Research: Solid Earth*, *121*, 6675–6697. https://doi.org/10.1002/2016JB012978

Foster, K., Dueker, K., Schmandt, B., & Yuan, H. (2014). A sharp cratonic lithosphere–asthenosphere boundary beneath the American Midwest and its relation to mantle flow. *Earth and Planetary Science Letters*, *402*, 82–89.

Gao, S. S., & Liu, K. H. (2014). Mantle transition zone discontinuities beneath the contiguous United States. *Journal of Geophysical Research: Solid Earth*, *119*, 6452–6468. https://doi.org/10.1002/2014JB011253

Gu, Y., Dziewonski, A. M., & Agee, C. B. (1998). Global de-correlation of the topography of transition zone discontinuities. *Earth and Planetary Science Letters*, *157*(1-2), 57–67.

Gu, Y. J., Dziewoński, A. M., & Ekström, G. (2003). Simultaneous inversion for mantle shear velocity and topography of transition zone discontinuities. *Geophysical Journal International*, *154*(2), 559–583.

Hansen, S. M., Dueker, K., & Schmandt, B. (2015). Thermal classification of lithospheric discontinuities beneath USArray. *Earth and Planetary Science Letters*, *431*, 36–47.

Hier-Majumder, S., & Tauzin, B (2017). Pervasive upper mantle melting beneath the western US. *Earth and Planetary Science Letters*, *463*, 25–35.

Hopper, E., & Fischer, K. M. (2015). The meaning of midlithospheric discontinuities: A case study in the northern US craton. *Geochemistry, Geophysics, Geosystems*, *16*, 4057–4083. https://doi.org/10.1002/2015GC006030

Houser, C., Masters, G., Flanagan, M., & Shearer, P. (2008). Determination and analysis of long-wavelength transition zone structure using ss precursors. *Geophysical Journal International*, *174*(1), 178–194.

James, D. E., Fouch, M. J., Carlson, R. W., & Roth, J. B (2011). Slab fragmentation, edge flow and the origin of the Yellowstone hotspot track. *Earth and Planetary Science Letters*, *311*(1-2), 124–135.

Kennett, B., & Engdahl, E. (1991). Traveltimes for global earthquake location and phase identification. *Geophysical Journal International*, *105*(2), 429–465.

Kind, R., Yuan, X., & Kumar, P. (2012). Seismic receiver functions and the lithosphere–asthenosphere boundary. *Tectonophysics*, *536*, 25–43.

Kumar, P., Kind, R., Yuan, X., & Mechie, J. (2012). USArray receiver function images of the lithosphere-asthenosphere boundary. *Seismological Research Letters*, *83*(3), 486–491.

Lekić, V., & Fischer, K. M. (2014). Contrasting lithospheric signatures across the western United States revealed by Sp receiver functions. *Earth and Planetary Science Letters*, *402*, 90–98.
Levander, A., & Miller, M. S. (2012). Evolutionary aspects of lithosphere discontinuity structure in the western US. *Geochemistry, Geophysics, Geosystems*, *13*, Q0AK07. https://doi.org/10.1029/2012GC004056
Levander, A., Schmandt, B., Miller, M., Liu, K., Karlstrom, K., Lee, C.-T. A., et al. (2011). Continuing Colorado plateau uplift by delamination-style convective lithospheric downwelling. *Nature*, *472*(7344), 461–465.
Liu, L., & Gao, S. S. (2018). Lithospheric layering beneath the contiguous United States constrained by S-to-P receiver functions. *Earth and Planetary Science Letters*, *495*, 79–86.
Moschetti, M., Ritzwoller, M., & Shapiro, N. (2007). Surface wave tomography of the western United states from ambient seismic noise: Rayleigh wave group velocity maps. *Geochemistry, Geophysics, Geosystems*, *8*, Q08010. https://doi.org/10.1029/2007GC001655
Obrebski, M., Allen, R. M., Pollitz, F., & Hung, S. H. (2011). Lithosphere-asthenosphere interaction beneath the western United States from the joint inversion of body-wave traveltimes and surface-wave phase velocities. *Geophysical Journal International*, *185*(2), 1003–1021.
Obrebski, M., Allen, R. M., Xue, M., & Hung, S. H. (2010). Slab-plume interaction beneath the Pacific Northwest. *Geophysical Research Letters*, *37*, L14305. https://doi.org/10.1029/2010GL043489
Pavlis, G. L. (2011). Three-dimensional wavefield imaging of data from the USArray: New constraints on the geometry of the Farallon slab. *Geosphere*, *7*(3), 785–801.
Pavlis, G. L., Sigloch, K., Burdick, S., Fouch, M. J., & Vernon, F. L. (2012). Unraveling the geometry of the Farallon plate: Synthesis of three-dimensional imaging results from USArray. *Tectonophysics*, *532*, 82–102.
Porritt, R. W., Allen, R. M., & Pollitz, F. F. (2014). Seismic imaging east of the Rocky Mountains with USArray. *Earth and Planetary Science Letters*, *402*, 16–25.
Ritsema, J., Ni, S., Helmberger, D. V., & Crotwell, H. P. (1998). Evidence for strong shear velocity reductions and velocity gradients in the lower mantle beneath africa. *Geophysical Research Letters*, *25*, 4245–4248.
Rondenay, S., Bostock, M., & Shragge, J. (2001). Multiparameter two-dimensional inversion of scattered teleseismic body waves 3. Application to the Cascadia 1993 data set. *Journal of Geophysical Research*, *106*, 30,795–30,807. https://doi.org/10.1029/2000JB000039
Rychert, C. A., & Shearer, P. M. (2009). A global view of the lithosphere-asthenosphere boundary. *Science*, *324*(5926), 495–498.
Schmandt, B., Dueker, K., Hansen, S., Jasbinsek, J. J., & Zhang, Z. (2011). A sporadic low-velocity layer atop the western us mantle transition zone and short-wavelength variations in transition zone discontinuities. *Geochemistry, Geophysics, Geosystems*, *12*, Q08014. https://doi.org/10.1029/2011GC003668
Schmandt, B., Dueker, K., Humphreys, E., & Hansen, S. (2012). Hot mantle upwelling across the 660 beneath Yellowstone. *Earth and Planetary Science Letters*, *331*, 224–236.
Schmandt, B., Jacobsen, S. D., Becker, T. W., Liu, Z., & Dueker, K. G. (2014). Dehydration melting at the top of the lower mantle. *Science*, *344*(6189), 1265–1268.
Schmandt, B., & Lin, F.-C. (2014). P and S wave tomography of the mantle beneath the United States. *Geophysical Research Letters*, *41*, 6342–6349. https://doi.org/10.1002/2014GL061231
Selway, K., Ford, H., & Kelemen, P. (2015). The seismic mid-lithosphere discontinuity. *Earth and Planetary Science Letters*, *414*, 45–57.
Shang, X., Hoop, M. V., & Hilst, R. D. (2012). Beyond receiver functions: Passive source reverse time migration and inverse scattering of converted waves. *Geophysical Research Letters*, *39*, L15308. https://doi.org/10.1029/2012GL052289
Shearer, P. M. (1990). Seismic imaging of upper-mantle structure with new evidence for a 520-km discontinuity. *Nature*, *344*(6262), 121–126.
Shearer, P. M. (1991). Constraints on upper mantle discontinuities from observations of long-period reflected and converted phases. *Journal of Geophysical Research*, *96*, 18,147–18,182. https://doi.org/10.1029/91JB01592
Shragge, J., Artman, B., & Wilson, C. (2006). Teleseismic shot-profile migration. *Geophysics*, *71*, SI221–SI229. https://doi.org/10.1190/1.2208263
Sigloch, K. (2011). Mantle provinces under North america from multifrequency P wave tomography. *Geochemistry, Geophysics, Geosystems*, *12*, Q02W08. https://doi.org/10.1029/2010GC003421
Tauzin, B., Bodin, T., Debayle, E., Perrillat, J.-P., & Reynard, B. (2016). Multi-mode conversion imaging of the subducted Gorda and Juan de Fuca plates below the North American continent. *Earth and Planetary Science Letters*, *440*, 135–146.
Tauzin, B., Van Der Hilst, R. D., Wittlinger, G., & Ricard, Y. (2013). Multiple transition zone seismic discontinuities and low velocity layers below western United States. *Journal of Geophysical Research: Solid Earth*, *118*, 2307–2322. https://doi.org/10.1002/jgrb.50182
Wang, Y., & Pavlis, G. L (2016). Roughness of the mantle transition zone discontinuities revealed by high-resolution wavefield imaging. *Journal of Geophysical Research: Solid Earth*, *121*, 6757–6778. https://doi.org/10.1002/2016JB013205
Yu, C., Zhan, Z., Hauksson, E., & Cochran, E. S (2017). Strong sh-to-love wave scattering off the southern california continental borderland. *Geophysical Research Letters*, *44*, 10,208–10,215. https://doi.org/10.1002/2017GL075213
Yuan, H., Romanowicz, B., Fischer, K. M., & Abt, D. (2011). 3-D shear wave radially and azimuthally anisotropic velocity model of the North American upper mantle. *Geophysical Journal International*, *184*(3), 1237–1260.
Zhao, C., Garnero, E. J., McNamara, A. K., Schmerr, N., & Carlson, R. W (2015). Seismic evidence for a chemically distinct thermochemical reservoir in Earth's deep mantle beneath hawaii. *Earth and Planetary Science Letters*, *426*, 143–153.
Zheng, Z., & Romanowicz, B. (2012). Do double SS precursors mean double discontinuities? *Geophysical Journal International*, *191*(3), 1361–1373.